Supplemental Material for: Membrane-based scanning force microscopy

David Hälg,[1,*] Thomas Gisler,[1,*] Yeghishe Tsaturyan,[2,3] Letizia Catalini,[2,4] Urs Grob,[1] Marc-Dominik Krass,[1] Martin Héritier,[1] Hinrich Mattiat,[5] Ann-Katrin Thamm,[1] Romana Schirhagl,[6] Eric C. Langman,[2,4] Albert Schliesser,[2,4] Christian L. Degen,[1] and Alexander Eichler[1]

[1] *Laboratory for Solid State Physics, ETH Zürich, 8093 Zürich, Switzerland.*
[2] *Niels Bohr Institute, University of Copenhagen, 2100 Copenhagen, Denmark.*
[3] *Present address: Pritzker School of Molecular Engineering, University of Chicago, Chicago, IL 60637, USA.*
[4] *Center for Hybrid Quantum Networks, Niels Bohr Institute, University of Copenhagen, 2100 Copenhagen, Denmark.*
[5] *Department of Physics, University of Basel, 4056 Basel, Switzerland.*
[6] *Department of Biomedical Engineering, Groningen University, 9713 AW Groningen, The Netherlands.*

S1. SETUP

Our instrument comprises a silicon nitride membrane (for which we assume a refractive index of 2.0), a commercial atomic force microscope (AFM) tip on a stepping and scanning stage, and an optical interferometer that is focused onto one of the membrane defects (Fig. S1). The laser spot is positioned on the mode with the help of a second motor stage, an optical microscope, and a visible 633 nm laser (see red spot in Fig. S1(b)). We center the interferometer on the defect in x and y before adjusting the lens-membrane distance to match the focal distance of the lens.

The scanning probe, shown in Fig. S1(c) and (d), is a commercial silicon AFM tip (OPUS 240AC-PP) with a nominal tip radius of < 25 nm and 25 nm Pt coating on each side. It is glued onto a custom metal needle with a conducting epoxy (EPO-TEK H20E). After the epoxy is cured, we break off the cantilever support chip to avoid unwanted surface interaction.

In addition to the laser and tip driving methods described in the main text, the membrane can be driven by a dither piezo embedded into the sample holder. If not indicated otherwise, the data shown in the SI was recorded with this piezo element as a drive.

S2. NONLINEARITY OF THE LOADED MEMBRANE

We characterized the nonlinearity of the loaded membrane resonator to assess the influence of sample loading on the mechanical nonlinearities. In Fig. S2(a) we show the membrane response to an electrical tip drive. The behavior is typical for a Duffing nonlinearity (nonlinear spring constant) [1]. We also performed ringdown measurements with large initial amplitudes to compare the nonlinearities to unloaded membranes. The ringdown in Fig. S2(b) only shows deviations from a single exponential fit at amplitudes approaching ≈ 10 nm, in agreement with previous studies on unloaded membranes [1]. The effect of these nonlinearities are already taken into account in our proposals for future spin detection measurements [2].

S3. SAMPLE PREPARATION

The large area of the membrane defect allows to deposit samples from a liquid suspension through a micropipette attached to a micromanipulator. Preceding the sample deposition, the membrane is cured with an UV Ozone Cleaner to eliminate organic contaminants and to increase the hydrophilicity of its surface. The custom micropipette consists of a hollow glass capillary that is sharpened with a NARISHIGE PC-10 puller (see inset Fig. S3(b)) and connected to a syringe. To achieve a sufficiently high flow, we manually break the capillary

* These authors contributed equally to this work.

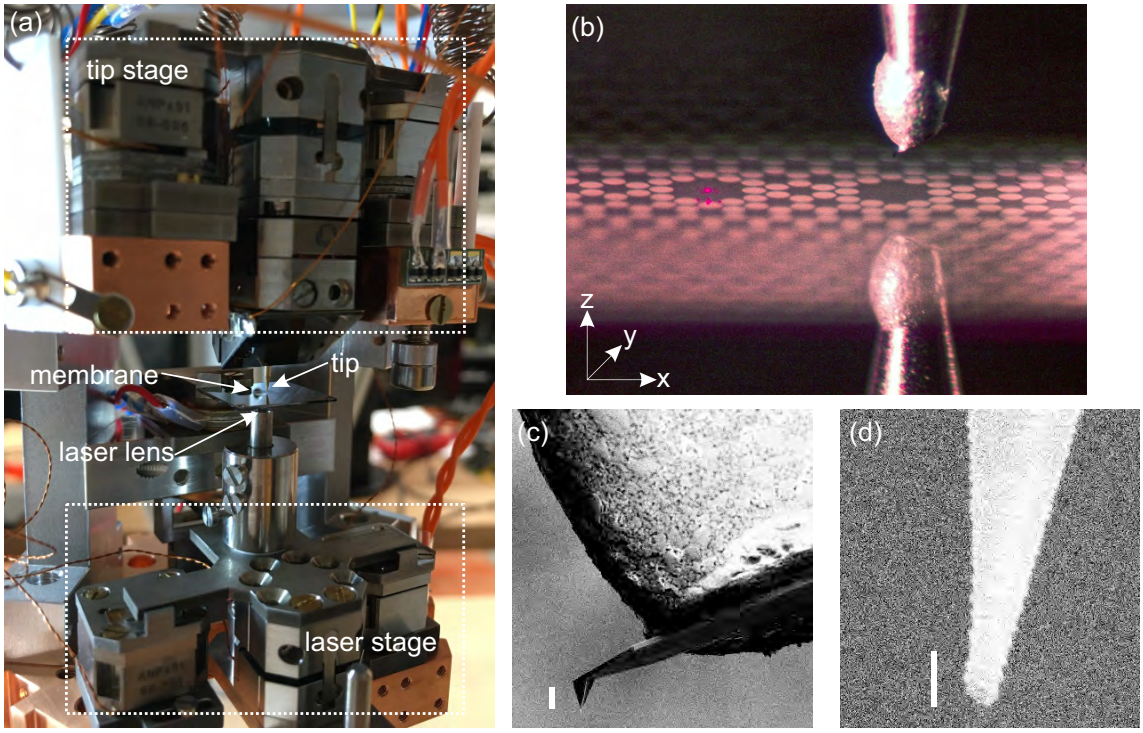

FIG. S1. **Components of scanning force microscopy stage.** (a) Custom microscope setup with scanning motors to move the tip (top stage) and the laser spot (bottom stage). (b) Optical microscopy image of a membrane mounted in the setup. The left defect mode is used for readout, while the right defect mode serves as a sample plate. (c)-(d) Scanning electron micrographs of the scanning tip used in the main text with scale bars of 10 µm in (c) and 100 nm in (d).

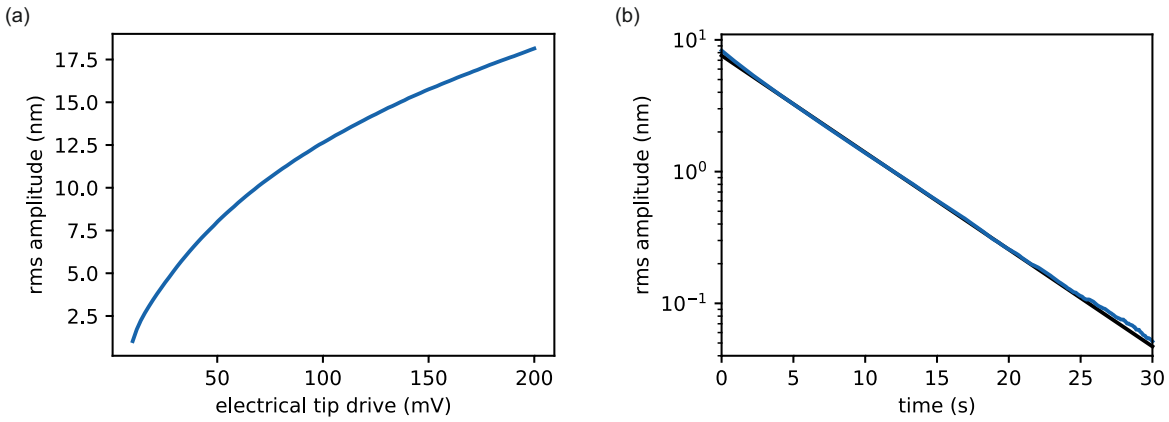

FIG. S2. **Nonlinearity of the loaded membrane resonator.** Shown in (a) is the vibration amplitude of the membrane as a function of the drive amplitude. The membrane was resonantly driven by an electrical ac tone applied over the tip. The tip-surface distance was >1 µm during this measurement. (b) The amplitude decay during a ringdown is approximately linear up to ≈ 10 nm, in agreement with previous studies on unloaded membranes [1]. The black line is an exponential fit.

tip off.

The syringe allows a controlled deposition of a suspension droplet with samples. Due to residues in the solvents, evaporated droplets leave an unwanted crystalline structures on the membrane. This can be partially avoided by retracting the solvent little by little back into the pipette. Experience has shown that a total impact time of 60 seconds before removing the residual

droplet is an appropriate compromise between the deposited amount of sample material and contamination. The membranes are surprisingly robust; however, the risk of structural damage increases with decreasing membrane thickness. The rate of a successful deposition that leaves the membrane intact varies from about 50 percent (for a thickness below 20 nm) to almost 100 percent (60 nm).

We have found that membranes treated in this way preserved quality factors up to 70 millions, whereas untreated membranes achieved up to 100 millions in our scanning force setup. The difference could be due to statistical spread, and we have no systematic evidence for a reduction of Q with the sample deposition.

For the work shown in the main text, we used two different types of samples simultaneously: commercially available gold nanoparticles (BBI SOLUTIONS) with a nominal mean diameter of 50 nanometers and tobacco mosaic viruses (TMV) cultivated within the group of Prof. C. Degen at ETH Zurich. The two sample types were applied consecutively (first gold, second TMV) with the procedure described above.

In future studies, the liquid dispersion technique may be improved by utilizing femtoliter droplets deposited with a hollow cantilever 'nanopipette', which may allow targeted placement of individual macromolecules. Dispersion of particles from gas with a nozzle could preserve even higher quality factors. Finally, shock freezing and drying by sublimation of biological samples is often used to avoid structural damage to the samples incurred through capillary forces during a conventional evaporation process. In our microscope, samples could be freeze-dried on a microscopic sample holder (such as a patterned silicon platelet) and then deposited on the membrane surface with a micromanipulator. We therefore see the potential for studying a wide range of samples with our membrane-based inverted scanning force microscope.

S4. FORCE SENSITIVITY OF AN UNLOADED SINGLE-DEFECT MEMBRANE

In the following, we present approach data from a second membrane without samples on the surface. This is a single-defect membrane, such that the scanning tip and laser interferometer spot had to be aligned carefully next to each other. Here we used a scanning tunnelling microscopy (STM) tip made from tungsten by electrochemical wet etching as a scanning probe.

As we can see in Fig. S4, the membrane retains its excellent force sensitivity in proximity to a scanning tip. An increase of the force noise can only be noticed below 50 nm distance, and the force noise stays at a very low level even for distance within the nanometer range.

In Fig. S5, we show the tip-sample non-contact friction calculated from the data in Fig. S4 (brown) and for a second data set with a drive of 10 μV (blue). Importantly, the data obtained with the two different driving strengths coincide, demonstrating that the dissipation is invariant with the driving force and the vibration amplitude.

S5. SCAN DATA PROCESSING AND ADDITIONAL SCAN DATA

The scans data in Fig. 3 of the main text and Fig. S6 were plane-leveled and Fig. 3(a) was additionally line averaged. The scale of the x and y coordinates were calculated with the piezo specifications from the ATTOCUBE data sheet. The measured TMV sample were used to calibrate the z movement of the ATTOCUBE scanner.

In Fig. S6 we show additional topography images obtained with a single-defect membrane and an etched tungsten tip.

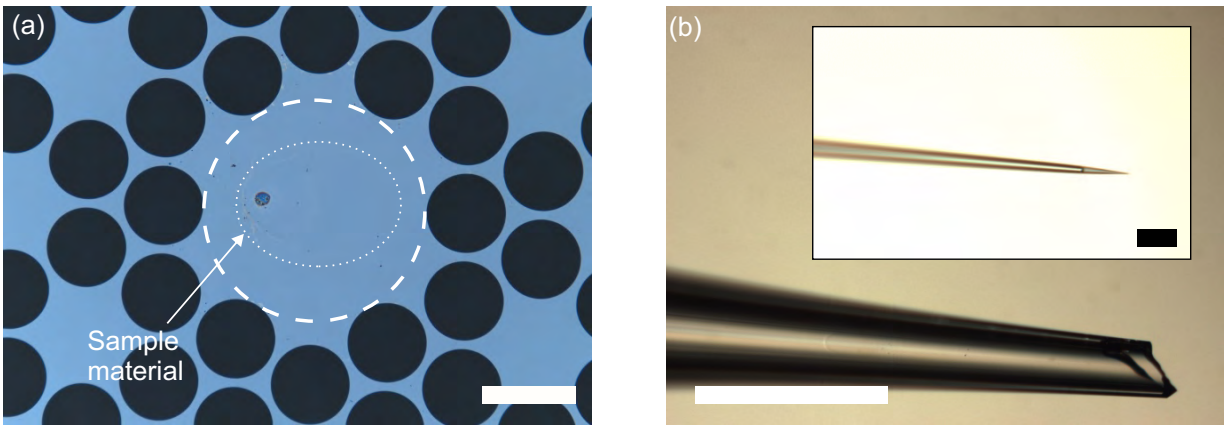

FIG. S3. **Sample Preparation.** Optical microscopy image (a) showing the membrane area with deposited samples. The image was taken with the double-defect membrane used for this work. The dashed line indicates the membrane defect, while the dotted line emphasises the outline of the deposited sample material. The lateral scale bar is 100 µm. (b) Glass capillary after and before (inset) breaking the tip off. The lateral scale bars are 50 µm.

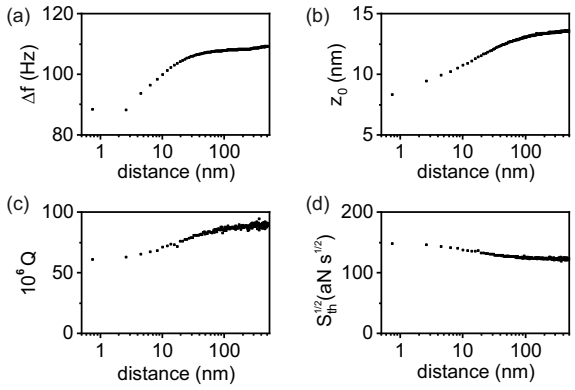

FIG. S4. **Tip approach with a single defect membrane and a tungsten tip.** (a)-(c) Shift of the measurement frequency, vibration amplitude, and quality factor measured as a function of tip-surface distance, respectively. The membrane is driven by a piezo element and has no sample loaded. (d) Intrinsic thermomechanical force noise calculated from the measured quantities with an effective mass of $m = 16$ ng [3].

S6. QUANTUM-LIMITED CAVITY READOUT OF MECHANICAL MOTION

To illustrate the potential for quantum-limited measurement of mechanical motion, Fig. S7 shows an optically measured mechanical displacement spectrum. It displays ponderomotive squeezing, that is, the optical quantum noise is reduced below the vacuum noise level (normalised to 1). This is a consequence of quantum correlations between mechanical motion and fluctuations of the optical field, which are generated when quantum fluctuations of radiation pressure set the membrane into motion. Such correlations can be exploited to measure mechanical motion with a sensitivity better than the standard quantum limit, as demonstrated with a membrane resonator in reference [4]. The membrane with which the data of Fig. S7 was recorded is similar (though not identical) to the one used in this work. Specifically, it was a single-defect membrane of 20 nm thickness and with a resonance frequency of ca. 1.1 MHz. Its motion was probed with an optical Fabry-Perot interferometer of 1.6 mm length and ca. 7000 Finesse, using 1.8 µW of laser light at a wavelength of 796 nm.

S7. SCANNING CAVITY

The implementation of a high-finesse Fabry-Perot interferometer in the scanning force microscope will increase the displacement sensitivity, which is essential for ultrasensitive force detection. Figure S8(a) illustrates the prospective geometry of a scanning cavity. The design benefits from the spatial separation of the sample defect and the optical readout defect (shown as two large maxima of the membrane displacement). Figure S8(b) shows the thermally driven spectrum of the symmetric mode of an unloaded double-defect membrane. It was measured

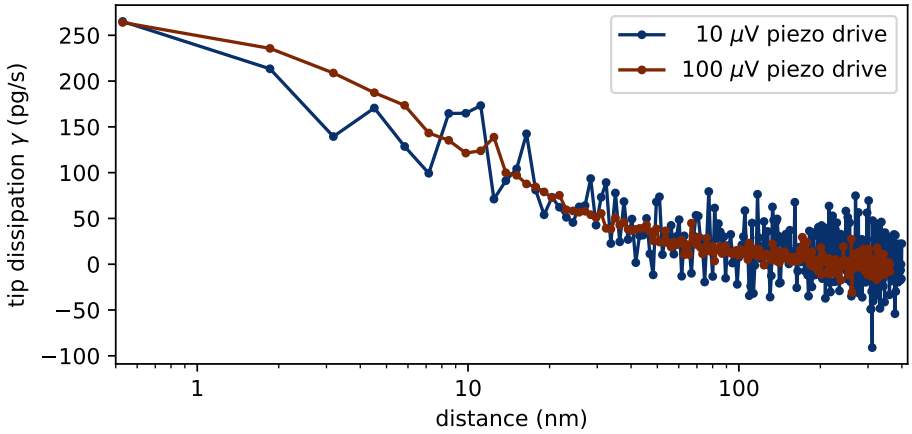

FIG. S5. **Dissipation induced by the presence of a scanning tip.** Data are calculated from ringdown measurements performed at different distances with two different piezo driving strengths. The average dissipation for large tip-surface distances is used as a baseline, and shaded areas mark the standard deviation of the corresponding uncertainty. These measurements were performed with the same membrane and tip as in Fig. S4.

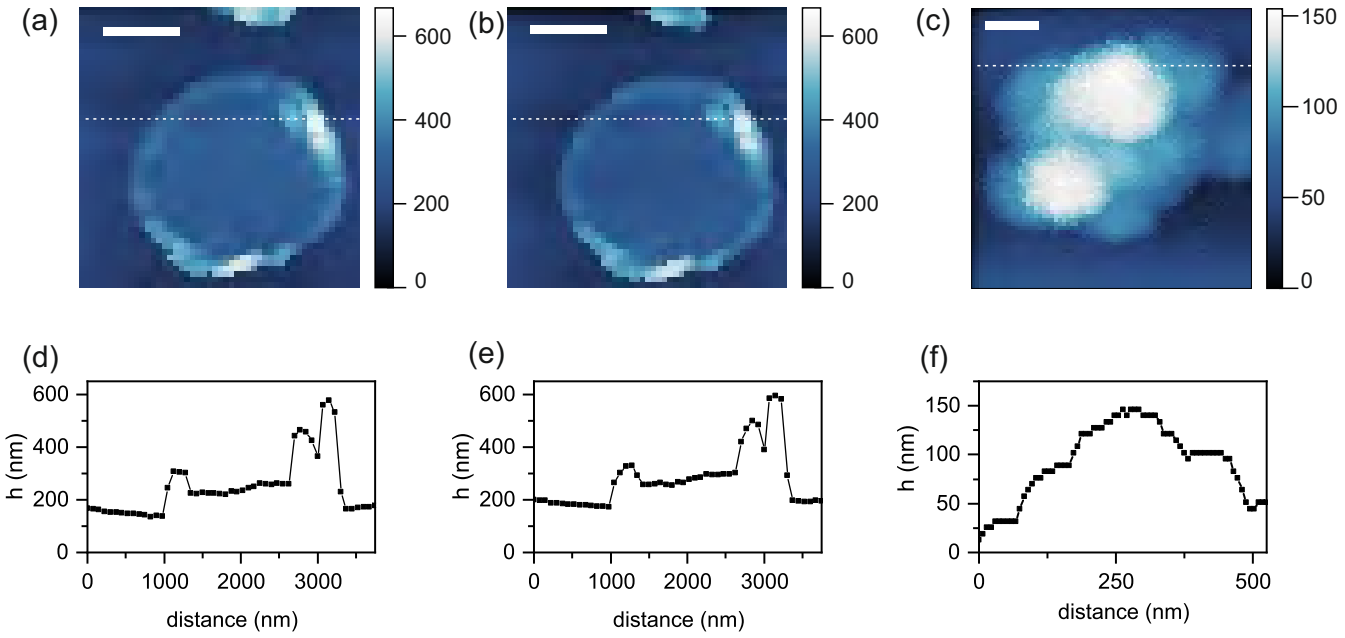

FIG. S6. **Topography images.** Scans of objects on single-defect membranes. Measurements were performed with piezo driving and with an STM tip made from tungsten. (a) Scan of a gold pad that was evaporated onto the membrane with a nominal height of 100 nm. Lateral scale bar is 1 µm. (b) Repetition of the scan in (a) to demonstrate the image reproducibility and low drift. No drift compensation was used for the entire measurement time of 26 hours. (c) Scan of a cluster of gold nanoparticles. Lateral scale bar is 100 nm. (d)-(f) Linescans extracted from (a)-(c), respectively, at the positions indicated by the dashed lines.

with a scanning cavity prototype where the scanning motors and tip were not yet implemented. The cavity measures 4.2 mm in length and has a Finesse of about 650. The displacement sensitivity is calibrated with two different methods: the left y-axis in Fig S8(b) was obtained by measuring the coupling between the light and the membrane, resulting in a sensitivity of 1.6×10^{-30} m^2/Hz; the right axis was obtained by using the thermal motion of the mechanical mode for calibration, resulting in 3.5×10^{-29} m^2/Hz. The thermal calibration assumes that

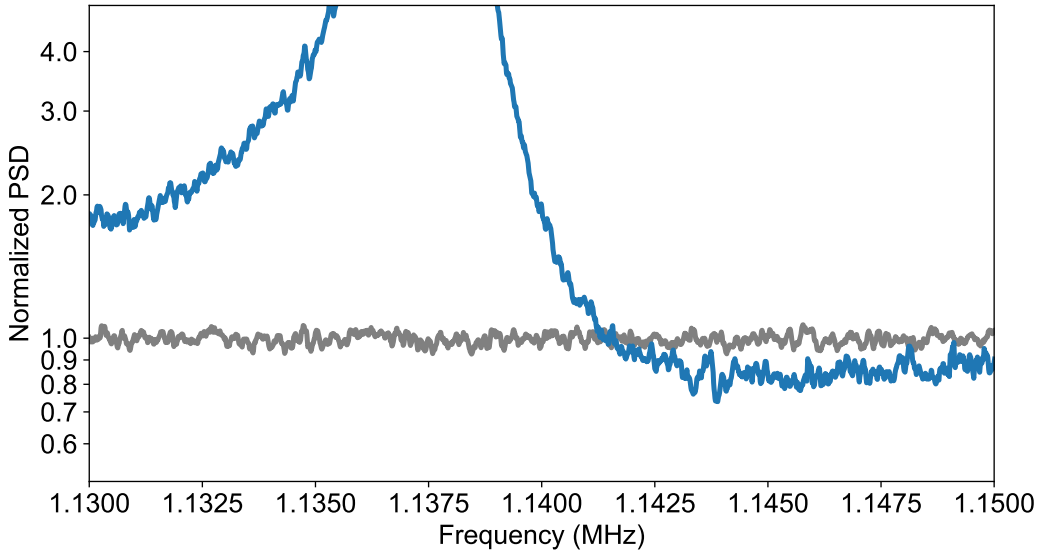

FIG. S7. **Ponderomotive squeezing of light.** The spectral density of the measured optical interferometer signal (blue) is reduced below the vacuum noise level (grey). This is the result of quantum correlations between mechanical motion and optical quantum fluctuations. The peak in the blue curve corresponds to the mechanical resonance of a membrane comparable to the one used in this work.

the beam spot is positioned at the maximum of the mechanical mode shape. This assumption may be wrong, resulting in an overestimation of the background noise and potentially explaining the discrepancy between the two calibration methods. The quality factor used for the calibration fit was determined by ringdown measurements.

S8. ENGINEERING OF LOW MASS DEFECTS

New phononic crystal/defect combinations are actively being designed and fabricated to increase Q/m and proportionally decrease the force noise. A fabricated single-defect membrane is presented in Fig. S9, demonstrating the principle structure behind one such new design. The phononic crystal is tapered down to a six-point trampoline resonator, engineered in such a way as to avoid extremes in the tensile stress in the connecting region. Conveniently, this design also reduces or eliminates non-essential mechanical modes within the bandgap and allows for the primary defect mode to be centered within the bandgap itself.

In Table S1, we compare the Q-factor and force sensitivity of the 'standard' design to a pair of new 'low-mass' designs defined by a critical dimension: the tether width of the trampoline arms. This critical dimension is what predominately determines the mode mass of the resonance, with its lower bound set by the processing steps of the fabrication resolution. The top section of the table combines measured Q-factors with simulated mode masses for initial fabrications made with 50 nm thick membranes. To obtain the rescaled values shown in the two bottom sections of the chart, standard scalings for soft-clamped membranes are used, namely $Q \propto (\text{thickness})^{-1} \times (\text{frequency})^{-2}$. Additionally, it is assumed that the quality factors will increase by a factor 3.5 when cooling from room temperature to cryogenic temperatures, as observed with previous devices.

The rescaled values for 1.6 MHz defect modes fabricated with 100 nm membranes are directly comparable to the survey results of typical designs conducted by Reetz et al. [7]. Our findings suggest a potential for significant improvement in force sensitivity over previous designs,

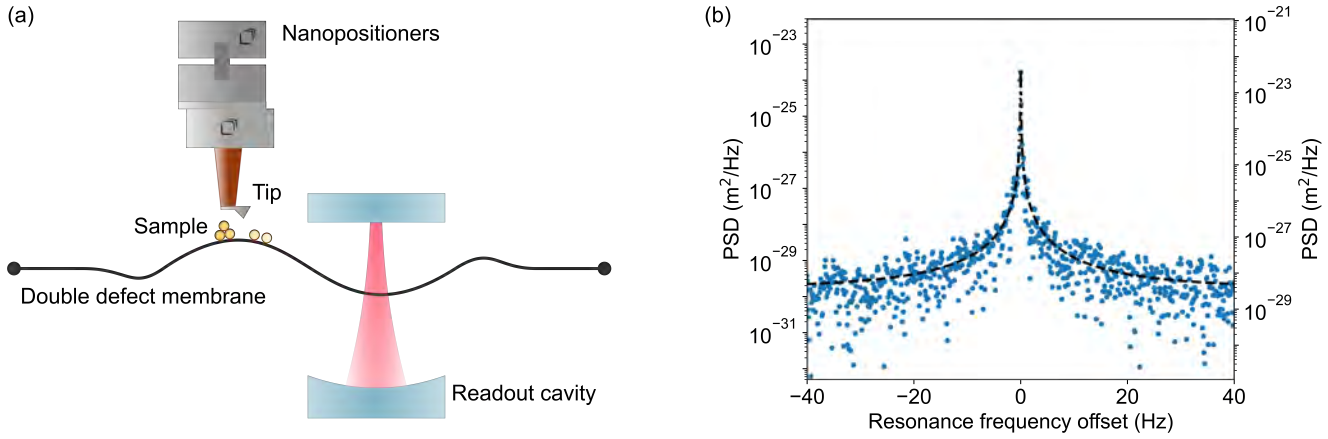

FIG. S8. **Proposed design and first measurements of a scanning cavity prototype.** (a) Schematic illustration of a scanning cavity a combination of a high precision optical readout cavity with a scanning tip. (b) Displacement power spectral density of the mechanical mode (1.44 MHz) measured with our first scanning cavity prototype at a laser power of 10 µW (1550 nm). The y-axes differ in the calibration method (left y-axis: via measured coupling, right y-axis: thermal calibration). The black dashed line indicates the fit used for thermal calibration.

	m	k	Q ($\times 10^6$)		$S_{\mathrm{th}}^{1/2}$ (aN/$\sqrt{\mathrm{Hz}}$)		
Design (thickness, frequency)	(pg)	(N/m)	300 K	$\leq$ 10 K	300 K	4 K	0.2 K
Fabricated (50 nm, 1.6 MHz)							
Standard	8000	809	58.0	—	150	—	—
Low Mass: 3 µm	600	61	41.5	—	49	—	—
Low Mass: 1 µm	100	10	15.9	—	32	—	—
Rescaled (100 nm, 1.6 MHz)							
Standard	16000	1620	29.0	120	300	18.6	2.08
Low Mass: 3 µm	1200	121	21.3	74	97	6.0	1.35
Low Mass: 1 µm	200	20	8.0	28	65	4.0	0.89
Rescaled (15 nm, 1.0 MHz)							
Standard	6000	237	470	1650	36.3	2.24	0.50
Low Mass: 3 µm	460	18	360	1250	11.5	0.71	0.16
Low Mass: 1 µm	77	3	140	480	7.54	0.47	0.10

TABLE S1. Comparing mass m, spring constant k, quality factor Q, and the single-sided force sensitivity of new designs to the standard defect design utilized in previous works [3–6]. For 'Low Mass' designs, the critical dimension (1 µm, 3 µm) corresponds to the width of tethers of the central trampoline defect.

with still a large parameter space to explore for optimization. With operational membranes expected to be 15 nm thick (or less), the final third of Table S1 provides optimistic predictions for state-of-the-art membranes utilizing these designs.

S9. ROLE OF DISPLACEMENT IMPRECISION AT FINITE FREQUENCY OFFSET

In Fig. S10, we show the impact of the displacement imprecision on the effective force noise of the membrane sensors used in this work as a function of frequency offset (from f_0). This becomes important, for instance, for the detection of nuclear spin signals with lifetime-limited

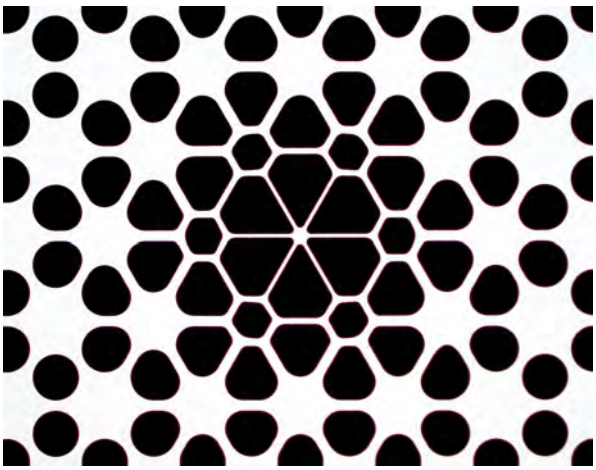

FIG. S9. Micrograph image of low-mass defect design being explored for enhanced force sensitiviy. The critical-dimension trampoline tethers are enlarged here, relative to the specific structures analyzed in Table S1.

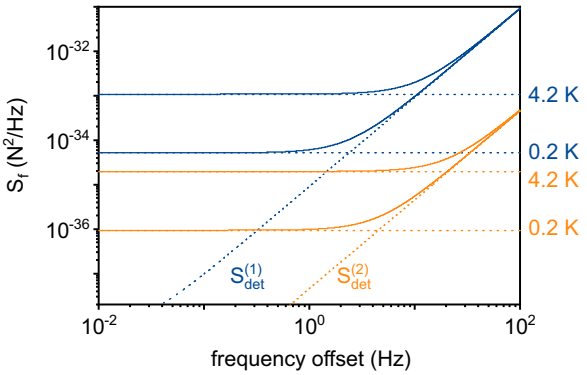

FIG. S10. **Effective force noise PSD.** Calculated apparent force noise $S_f = S_{\rm th} + S_{\rm det}/|\chi_{\rm m}(f)|^2$ consisting of thermomechanical force noise $S_{\rm th}$ (horizontal dotted lines) and displacement imprecision $S_{\rm det}$ (diagonal dotted lines), where $\chi_{\rm m}(f)$ is the mechanical susceptibilty. Blue solid lines correspond to the predicted performance of the device used in this work at 4.2 K and 0.2 K with $S^{(1)}_{\rm det} = 2\times10^{-28}$ m^2/Hz (single-sided convention). Orange solid lines are calculated for a device tested without force scanning, with $m = 2$ ng, $f_0 = 1.35$ MHz, and $Q = 2\times10^8$ [1]. For this device, we project the numbers obtained when using an optical cavity with $S^{(2)}_{\rm det} = 10^{-30}$ m^2/Hz for readout.

spectral widths (e.g. 50 Hz for hydrogen signals in a typical NanoMRI measurement). For the parameters of this sensor, quantum backaction effects are not yet relevant.

S10. GROWTH OF TOBACCO MOSAIC VIRUSES

Tobacco mosaic viruses (TMV) were produced by infected tobacco plants [8]. Young plants are grown from the seeds and can be easily infected when they have approximately 4 leaves. At this stage, they are strong enough to survive the treatment but not to withstand the virus infection. Infecting is done by rubbing a small area on a leaf with fine sand and dropping the virus solution on the injured area. The success of infection can be confirmed by optical examination of the leaves after a few weeks. Leaves on plants suffering from the mosaic sickness tend to be smaller and have a mosaic structure consisting of light and dark green patches. The infected plants are then grown for several months until they are ready to be harvested. In order to extract the viruses, the vein-free parts of infected tobacco leaves are crushed in liquid nitrogen and stored for further usage at $-80°$ C. The dried powder is re-suspended in buffer containing 2-mercaptoethanol. The mixture is filtered through a large-pored cheese cloth to remove large parts. Then, butanol is added to the filtrate and stirred, followed by centrifugation. The supernatant is removed and NaCl and poly(ethylene glycol) are added to the suspension to precipitate the proteins. The suspension is centrifuged again and the supernatant is discarded. The pellet is re-suspended in KH2PO4/K2HPO4 buffer containing Triton X-100. Finally, a density gradient centrifugation is performed using a sucrose pad (buffered 25 % percent sucrose). The pellet is washed and centrifuged until the required purity is obtained. The protein concentration can be determined by UV-visible spectroscopy. The success of the purification process was confirmed by observing the characteristic rod-shaped viruses under a scanning electron microscope and a conventional atomic force microscope.

[1] L. Catalini, Y. Tsaturyan, and A. Schliesser, Soft-clamped phononic dimers for mechanical sensing and transduction, Phys. Rev. Applied **14**, 014041 (2020).

[2] J. Košata, O. Zilberberg, C. L. Degen, R. Chitra, and A. Eichler, Spin detection via parametric frequency conversion in a membrane resonator, Phys. Rev. Applied **14**, 014042 (2020).

[3] Y. Tsaturyan, A. Barg, E. S. Polzik, and A. Schliesser, Ultracoherent nanomechanical resonators via soft clamping and dissipation dilution, Nature Nanotechnology **12**, 776 (2017).

[4] D. Mason, J. Chen, M. Rossi, Y. Tsaturyan, and A. Schliesser, Continuous force and displacement measurement below the standard quantum limit, Nature Physics **15**, 745 (2019).

[5] M. Rossi, D. Mason, J. Chen, Y. Tsaturyan, and A. Schliesser, Measurement-based quantum control of mechanical motion, Nature **563**, 53 (2018).

[6] J. Chen, M. Rossi, D. Mason, and A. Schliesser, Entanglement of propagating optical modes via a mechanical interface, Nature Communications **11**, 1 (2020).

[7] C. Reetz, R. Fischer, G. Assumpção, D. McNally, P. Burns, J. Sankey, and C. Regal, Analysis of membrane phononic crystals with wide band gaps and low-mass defects, Physical Review Applied **12**, 10.1103/physrevapplied.12.044027 (2019).

[8] G. M. Birnbaumer, P. A. Lieberzeit, L. Richter, R. Schirhagl, M. Milnera, F. L. Dickert, A. Bailey, and P. Ertl, Detection of viruses with molecularly imprinted polymers integrated on a microfluidic biochip using contact-less dielectric microsensors, Lab Chip **9**, 3549 (2009).